scientific reports

Check for updates

OPEN

Bulk single crystal growth and scintillation properties of Ce and Mg co-doped Y3Ga3Al2O12 for advanced X-ray imaging

Hisato Suezumi[1,2]✉, Kei Kamada[3,4]✉, Liudmila Gushchina[3], Masao Yoshino[2,3], Kyoung Jin Kim[3,4], Satoshi Ishizawa[2,3], Rikito Murakami[2,3], Yasuhiro Shoji[3], Yuui Yokota[2,4], Hiroki Sato[2,4], Takashi Hanada[2], Alena Beitlerova[5], Martin Nikl[5] & Akira Yoshikawa[2,3,4]

In this study, the Czochralski (Cz) growth and scintillation properties of 1-inch diameter $Y_3Ga_3Al_2O_{12}$ (YAGG) single crystals co-doped with Ce and Mg were investigated. The growth atmosphere was optimized to suppress gallium oxide evaporation and iridium precipitation on the melt surface. The segregation behavior of the cations, including Ce and Mg, was systematically examined using electron probe microanalysis and inductively coupled plasma atomic emission spectrometry. The grown YAGG: Ce, Mg crystals outperformed commercial $Gd_3Ga_3Al_2O_{12}$:Ce, demonstrating a high light yield of 46,700 photons/MeV, an energy resolution of 8.5–11.4% at 662 keV, low afterglow, and a rapid decay time of ~ 50 ns. In addition, the Y K-edge lies outside the diagnostic X-ray energy range, underscoring the suitability of YAGG: Ce, Mg for photon-counting computed tomography applications. These results demonstrate the feasibility of producing large, high-performance YAGG: Ce, Mg crystals using the Cz method and establish a foundation for further improvements through the optimization of Ce and Mg concentrations and scaling of crystal size.

Keywords Photon-counting computed tomography, Czochralski method, Scintillation material, Inch-scale single crystal, Mg co-doping, Afterglow

Scintillators are essential functional materials for radiation detection and play crucial roles in medical diagnostics, nondestructive testing, security screening, and high-energy physics. In the medical field, photon-counting computed tomography (PCCT) has emerged as a next-generation X-ray imaging technology that offers an improved signal-to-noise ratio[1], material decomposition capability[2], multi-energy imaging[3], and reduced radiation dose[4,5] compared with conventional energy-integrating CT systems. These advantages have created a strong demand for scintillator materials specifically optimized for the stringent performance requirements of PCCT detectors. PCCT imposes fundamentally four key requirements on scintillators for practical implementation: (ⅰ) high light yield to ensure adequate energy resolution, (ⅱ) fast decay and minimal afterglow to suppress pulse pile-up and preserve accurate energy-bin discrimination, (ⅲ) absence of K-edge absorption within the 20–100 keV diagnostic X-ray range, which otherwise produces escape-peak artifacts and spectral distortion, and (ⅳ) centimeter-scale scintillation uniformity and stable producibility, which are indispensable for mass production and integration into multi-channel Photon-counting detectors (PCDs)[6–9].

The performance of scintillator-based PCDs depends primarily on the intrinsic properties of the scintillator crystal. Owing to their optical transparency, compositional tunability, and chemical stability, Ce-doped garnet-type oxides are among the most promising scintillator candidates. Among these, $Gd_3Ga_3Al_2O_{12}$:Ce (GAGG: Ce) has been extensively studied because of its high light yield (~ 56,000 photons/MeV), relatively fast decay constants (76 and 826 ns), and high stopping power, making it one of the most successful commercial scintillators in recent years[10–12]. Although Mg co-doping reduces the light yield to ~ 35,000 photons/MeV, it accelerates the decay components to 51 and 173 ns[13]. However, the Gd K-edge at ~ 50 keV, which lies within the diagnostic

[1]Graduation School of Engineering, Tohoku University, 6-6-2 Aramaki Aoba-ku, Sendai 980-8579, Japan. [2]Institute for Materials Research (IMR), Tohoku University, 2-1-1 Katahira, Aoba-ku, Sendai 980-8577, Japan. [3]C&A corporation, 1-16-23, ichibancho, Aoba-ku, Sendai 980-0811, Japan. [4]New Industry Creation Hatchery Center (NICHe), 6-6-10 Aoba, Aramaki, Aoba-ku, Sendai 980-8579, Japan. [5]Institute of Physics of the Czech Academy of Sciences, Cukrovarnicka 10, Prague 16200, Czech Republic. ✉email: suezumi.hisato.q3@dc.tohoku.ac.jp; kei.kamada.c6@tohoku.ac.jp

X-ray energy window (20–100 keV), produces strong escape peaks that critically limit energy discrimination in PCCT[2,14,15]. In addition, slow scintillation components and afterglow induce pulse pile-up, degrading the count-rate performance of PCDs[15]. Furthermore, Gd^{3+} ions introduce 4f–4f transitions that interfere with co-dopants such as Tb^{3+}, complicating energy-transfer processes[16–20].

These drawbacks have motivated the search for alternative host lattices, with yttrium-based garnets $Y_3(Ga, Al)_5O_{12}$:Ce (YAGG: Ce) emerging as promising candidates. The Y K-edge at 17 keV, well below the diagnostic energy window, avoids the spectral interference inherent to Gd-based materials[21]. Additionally, the Ga/Al ratio in YAGG can be tuned to optimize the bandgap and scintillation efficiency. Previous studies have shown that Mg co-doping suppresses the negative influence of shallow trap states near the conduction band, increasing the light yield and accelerating the decay. Kamada et al. reported that $Y_3Ga_3Al_2O_{12}$:Ce, Mg (YAGG: Ce, Mg) crystals grown via the micro-pulling-down (μ-PD) method exhibited a light yield of ~ 38,800 photons/MeV and a decay time below 55 ns, although key PCCT-relevant properties such as energy resolution and afterglow were not evaluated[22].

For practical applications, large-diameter, uniform bulk single crystals with stable scintillation properties are essential. Garnet-type oxide scintillators such as GAGG[13], $(Lu, Y)_2SiO_5$ (LYSO)[23], and $(La, Gd)_2Si_2O_7$ (La-GPS)[24] are routinely produced as 2–4-inch boules on an industrial scale using the Czochralski (Cz) method. While μ-PD is valuable for compositional exploration, it is intrinsically limited to millimeter-scale crystal growth; thus, scaling promising compositions requires bulk-growth techniques such as Cz.

In garnet materials, the melting point strongly depends on the elemental composition: approximately 2010 °C for $Lu_3Al_5O_{12}$[25], 1970 °C for $Y_3Al_5O_{12}$[26], and 1740 °C for $Gd_3Ga_5O_{12}$[27], increasing with higher Lu, Y, or Al content. Gallium-containing garnets exhibit substantial Ga_2O_3 evaporation at high temperatures. In μ-PD growth, crystals are grown within a few hours, minimizing Ga loss. In contrast, the Cz method requires 7–10 days to grow a bulk single crystal—during which the melt is continuously exposed to high temperatures—resulting in markedly increased Ga evaporation, composition drift, and severe oxidation and degradation of the iridium crucible.

These issues were clearly demonstrated in attempts to grow $Lu_2Gd_1Ga_3Al_2O_{12}$ (LGAGG) via the Cz method[28]. Although LGAGG was identified as a promising scintillator through μ-PD screening due to its high density and fast decay characteristics[10,11], the high Lu/Gd content implies an even higher melting point than GAGG. During Cz growth, Ga evaporation led to composition changes, secondary-phase precipitation, and increased turbidity as crystallization proceeded, causing the light yield to deteriorate. Luminescence was almost completely lost once the solidification fraction reached 30%. Given that YAGG is expected to exhibit a similarly high melting point, analogous issues—such as detrimental effects on crystal growth and nonuniformity in scintillation properties—must be carefully considered.

Segregation behavior also differs significantly between μ-PD and Cz growth. In μ-PD, segregation coefficients along the growth direction are theoretically close to unity for oxide garnets[29,30], resulting in nearly uniform composition. In contrast, Cz growth exhibits much smaller segregation coefficients for dopants such as Ce and Mg —reported as 0.42 and 0.021, respectively, in GAGG[31]—and even host elements show measurable segregation. These differences lead to compositional gradients and corresponding fluctuations in scintillation performance along the boule, posing major challenges for the development of new scintillator materials.

In this study, we investigate whether Ga_2O_3 evaporation, dopant segregation, and crucible degradation constitutes critical issues for the Cz growth of YAGG, and evaluates the extent to which these challenges can be mitigated through optimized growth conditions aimed at practical implementation and mass production. We further assess how composition fluctuations arising from dopant segregation and Ga evaporation influence the uniformity of scintillation properties—including light yield, decay time, energy resolution, radioluminescence (RL) spectra, and afterglow—along the growth direction of the produced crystal.

This work therefore provides the first experimental demonstration that YAGG: Ce, Mg can be grown as inch-scale, compositionally and functionally uniform single crystals by the Cz method, overcoming the limitations of previous μ-PD studies and establishing its feasibility as a practical scintillator for PCCT.

Materials and methods

A $(Y_{3-x-y}Ce_xMg_y)Ga_3Al_2O_{12}$ crystal was grown using the Cz method ($x = 0.01$, $y = 0.006$). Hereafter, $(Y_{2.984}Ce_{0.01}Mg_{0.006})Ga_3Al_2O_{12}$ is referred to as YAGG: Ce, Mg. High-purity (4 N) CeO_2, MgO, Y_2O_3, b-Ga_2O_3, and a-Al_2O_3 powders were prepared as starting materials. The mixed raw materials were sintered at 1500 °C in air. Crystal growth was performed using an Ir crucible with an inner diameter of 48 mm and $<100>$ $Y_3Al_5O_{12}$ (YAG: Ce) single crystals as seeds. The pulling and rotation rates were set to 0.7 mm/h and 10.0 rpm, respectively, and the crystal shape was controlled using an automatic diameter control (ADC) system. The growth atmosphere was maintained under N_2 with 25% CO_2 and Ar with 2% O_2 to suppress Ga evaporation. The grown crystals were sectioned into seven parts according to the crystallization ratio, cut into $5 \times 5 \times 1$ mm specimens, and mirror polished prior to analysis.

Powder X-ray diffraction (XRD; D8 DISCOVER, Bruker) with Cu Kα radiation was used to examine the phases of the grown samples. The acceleration voltage and current were 40 kV and 40 mA, respectively. To investigate the segregation behavior along the crystal growth direction, electron probe microanalysis (EPMA; JXA-8530 F, JEOL) with wavelength dispersive spectrometry (WDS) was performed for four cations: Y, Ce, Ga, and Al. In addition, inductively coupled plasma atomic emission spectrometry (ICP-AES; Thermo Fisher Scientific Inc., Waltham, MA, United States) was conducted to determine the concentrations of the five cations, including Mg, at each crystallization ratio.

RL spectra were recorded using an SR-163 spectrometer (Andor Technology) equipped with a CCD detector DU-420OE (Andor Technology). The measurements were performed under X-ray irradiation (40 kV, 20 mA) at an acquisition rate of 10 spectra per second. Scintillation light was collected using a photomultiplier tube (PMT;

R7600-200, Hamamatsu Photonics K.K., Hamamatsu, Japan) operated at 700 V. A 10 MBq ^{137}Cs source was positioned at a distance of 5 cm. Signals from the PMT were amplified using a spectroscopy amplifier (MSCF-16, mesytec GmbH & Co. KG, Putzbrunn, Germany) and digitized using a peak digital converter (PDC; A3400, NIKI GLASS Co., Ltd., Tokyo, Japan). The afterglow was measured using a custom-made spectrofluorometer 5000 M (Horiba Jobin Yvon), with steady-state excitation provided by an X-ray tube with a Mo anode (40 kV, 15 mA, Seifert GmbH), which was cut off at approximately 72 ms on the X-axis of the graph. A single-grating monochromator and a PCD TBX-04 (IBH, Scotland) were used for detection. Scintillation decay curves were recorded using a digital oscilloscope (RTB2004, Rohde & Schwarz GmbH & Co. KG, Munich, Germany). Considering that the YAGG: Ce, Mg scintillation decay contains two components, the experimental data were fitted using the sum of two exponential functions, I(t), where τ_1 and τ_2 represent the decay times of the fast and slow components, respectively.

$$I(t) = A_1 exp\left(\frac{-t}{\tau_1}\right) + A_2 exp\left(\frac{-t}{\tau_2}\right) + const.$$

Results and discussion

For the mass production of GAGG: Ce single crystals, a mixed atmosphere of Ar with 30% CO_2 was employed to minimize gallium oxide evaporation and Ir crucible degradation. The same atmospheric conditions were initially applied to the growth of the YAGG: Ce, Mg crystals. The results of the initial trial, conducted under a mixed atmosphere of N_2 and 25% CO_2, are shown in Fig. 1a. A metallic precipitate is visible on the crystal surface, with EPMA analysis identifying it as Ir. The growth process was suspended because of instability in crystal diameter control by the ADC system, caused by Ir film deposition on the melt surface and its adhesion to the crystal. Based on prior experience with GAGG: Ce growth, Ir deposition was considered to result from oxide evaporation. Moreover, in the Cz growth of β-Ga_2O_3 single crystals, several parameters such as temperature distribution, growth rate, rotation speed, crucible geometry, and oxygen partial pressure determine the crystal quality. Among them, precise control of the oxygen partial pressure is essential to suppress the decomposition and evaporation of Ga_2O_3 and to prevent oxidation and degradation of the Ir crucible. Therefore, maintaining an optimal oxygen partial pressure is indispensable for achieving thermochemical stability during crystal growth[32]. To mitigate gallium oxide evaporation, a second trial was conducted under an Ar + 2% O_2 mixed atmosphere. As shown in Fig. 1b, a 1-inch diameter YAGG: Ce, Mg crystal with a body length of 80 mm was successfully obtained. Although Ir film formation on the melt surface was suppressed compared with the first trial, it still led to seeding instability, requiring manual intervention for crystal shape control. After the initial shoulder growth was manually adjusted, the process was switched to ADC to continue the crystal growth. Despite a sudden fluctuation in crystal diameter caused by iridium deposition, a YAGG: Ce, Mg crystal with a 1-inch diameter and 80 mm body length was successfully grown. Figure 1c shows the powder XRD results for phase identification of the samples. Owing to the large sample size, phase identification was performed at three positions: the seed side, central region, and tail side. The results confirm that the sample consisted of a single cubic phase with space group Ia-3d, exhibiting high crystallinity and phase purity.

To evaluate cation segregation from the tail side to the seed side, line analysis was performed in the central region of the sample using EPMA at intervals of 0.2 mm for four cations: Ce, Y, Ga, and Al. To confirm the segregation behavior of Mg, seven points were selected at equal intervals from the seed side to the tail side, and their concentrations were examined using ICP-AES. Figure 2 shows the detailed compositional profiles obtained along the growth direction of the YAGG: Ce, Mg single crystal, where C_s and C_0 represent the actual and nominal compositions, respectively. The average solidification fraction (g) was approximately 0.46, with g defined by the following equation:

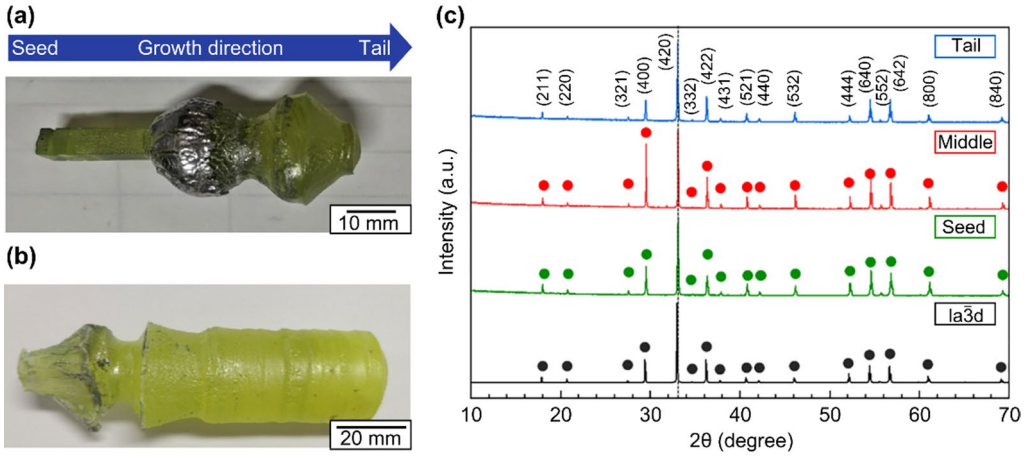

Fig. 1. Photographs of YAGG: Ce, Mg crystals grown (**a**) under N_2 + 25% CO_2 and (**b**) Ar + 2% O_2 atmospheres. (**c**) XRD patterns of YAGG: Ce, Mg at the tail, middle, and seed positions.

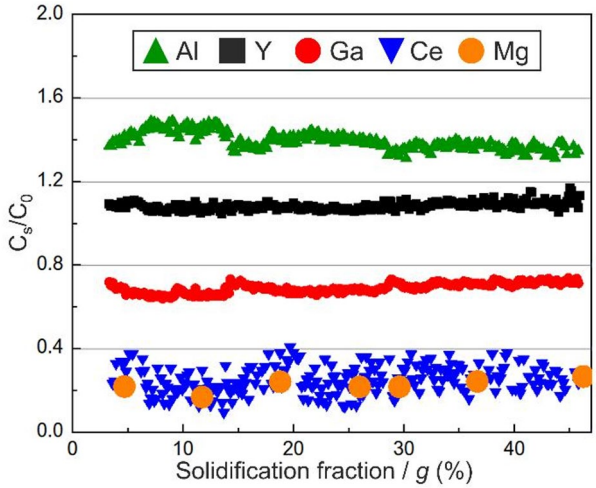

Fig. 2. Compositional distribution along the growth direction of the YAGG: Ce, Mg crystal.

$$g = \frac{\text{Mass of solidified part}}{\text{Total mass of starting raw material in the crucible}}$$

These results indicate that the cation distribution was homogeneous throughout the sample, with no significant deviation in chemical composition across the crystal. Therefore, the successful growth of a 1-inch diameter YAGG: Ce, Mg single crystal with uniform chemical composition was achieved. In addition, slight disturbances in the linearity of the compositional distribution can be observed at approximately g = 0.03, 0.15, and 0.3, corresponding to the positions in Fig. 1b where irregularities in the crystal diameter occurred. This suggests that deviations in the pulling rate and temperature control during crystal growth disrupted melt convection, leading to local fluctuations in the cation distribution. The effective segregation coefficients (k_{eff}) of Al, Y, Ga, Ce, and Mg were calculated using the following equation:

$$C_s/C_0 = k_{eff}\,(1-g)^{k_{eff}\,-\,1}$$

The k_{eff} values of Al, Y, Ga, Ce, and Mg are 1.53, 1.10, 0.62, 0.25, and 0.19, respectively. The effective segregation coefficient indicates the ease with which each cation is incorporated into the crystal. These results show that Al and Y, with $k_{eff} > 1$, were preferentially incorporated into the YAGG: Ce, Mg crystal, whereas Ga, Ce, and Mg, with $k_{eff} < 1$, were relatively less incorporated. The effective segregation coefficient of Ce (0.25) is comparable to that reported for GAGG: Ce, Mg grown using the Cz method (0.42)[31], indicating that Ce incorporation into the crystal is similar between the two hosts. In contrast, the effective segregation coefficient of Mg for GAGG: Ce, Mg is 0.021, whereas that for YAGG: Ce, Mg is 0.19, revealing that Mg incorporation is approximately ten times higher in YAGG: Ce, Mg. This difference in effective segregation coefficients can be explained by the differences in the ionic radii of the cations. Considering that previous studies performed crystal growth under the assumption that Ce and Mg substitute the dodecahedral Y site, the present crystals were grown using the same approach[20]. Accordingly, if the dopants in the crystal are assumed to occupy the dodecahedral sites, the ionic radii of the respective cations at these sites are 89 pm (Mg^{2+}), 105.3 pm (Ga^{3+}), and 101.9 pm (Y^{3+}). The ionic radius difference in GAGG: Ce, Mg is $R_{Gd} - R_{Mg}$ = 16.3 pm, whereas that in YAGG: Ce, Mg is $R_Y - R_{Mg}$ = 12.9 pm[33]. These results suggest that Mg^{2+} is more readily incorporated into YAGG: Ce, Mg, where the ionic radius difference with the host cation is smaller, explaining the observed difference in the effective segregation coefficient. Furthermore, given that the ionic radius of Ce^{3+} at the dodecahedral site is 114.3 pm, the ionic radius difference in GAGG: Ce, Mg is $R_{Ce} - R_{Gd}$ = 9 pm, whereas that in YAGG: Ce, Mg is $R_{Ce} - R_Y$ = 12.4 pm. The larger ionic radius difference at the Y site suggests that Ce is less likely to be incorporated. However, considering that Mg^{2+} is readily incorporated, Ce may be more easily incorporated when it coexists as Ce^{4+} near the Mg^{2+} sites, providing charge compensation.

Figure 3 shows the RL spectra of the YAGG: Ce, Mg crystal at room temperature at various positions from the seed to the tail side. Broad emission peaks can be observed at approximately 505–510 nm at all positions. This indicates the luminescence characteristics in response to radiation are uniform throughout the entire crystal along the crystal growth direction. However, previous studies on GAGG have found that the Ga concentration in the crystal affects the position of the Ce^{3+} $5d_1$ energy level relative to the conduction band minimum (CBM), and a decrease in Ga concentration shifts the $5d_1$ energy level toward lower energy[34–36] while the substitution of Gd by Y shows the opposite shift[37]. In the present study, ICP-AES analysis revealed a composition of $Y_{2.997}Ce_{0.001}Mg_{0.002}Ga_{2.263}Al_{2.737}O_{12}$, indicating a deficiency of Ga compared with the nominal composition. This deficiency can be attributed to Ga evaporation and segregation behavior. Jointly, this reduced Ga content and complete substitution of Gd by Y, shifted the $5d_1$-4f radiative transition of Ce^{3+} towards 505–510 nm.

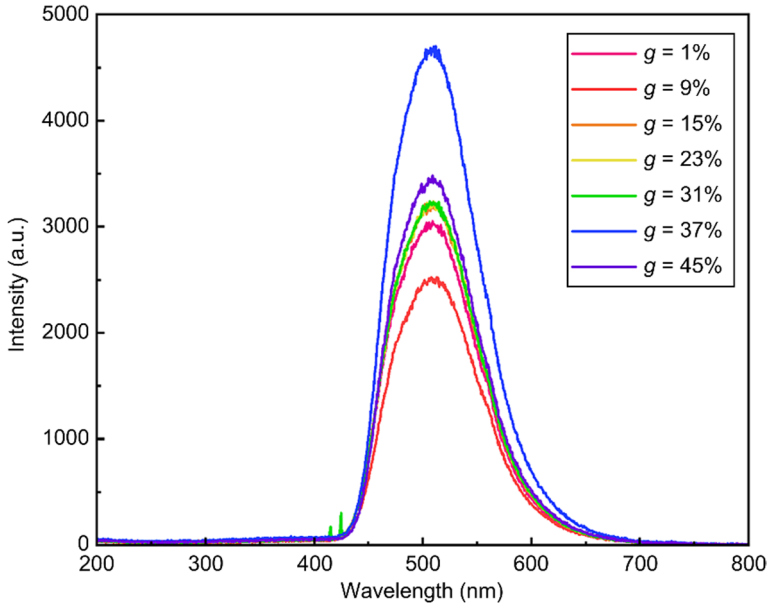

Fig. 3. RL spectra of YAGG: Ce, Mg at various positions.

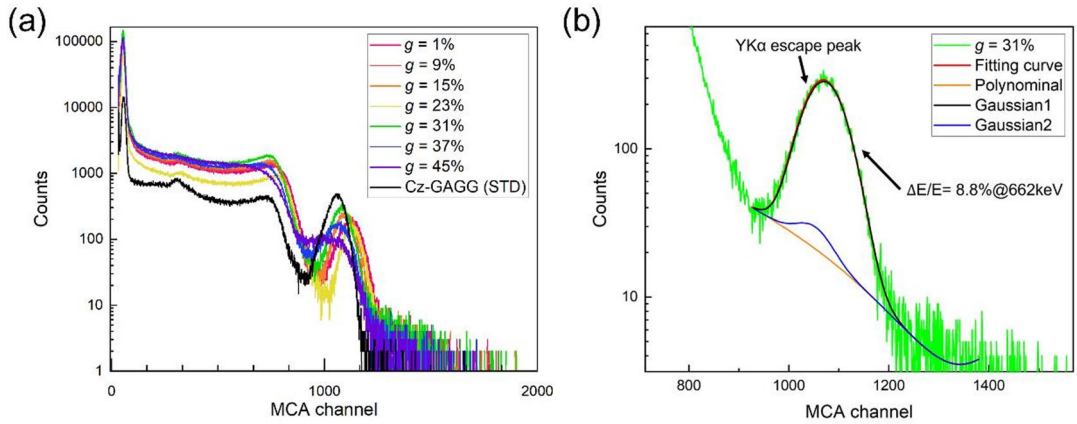

Fig. 4. (**a**) ^{137}Cs-induced pulse-height spectra of YAGG: Ce, Mg scintillators at various positions. Cz-grown GAGG: Ce was used as a reference. (**b**) Fitting result of the energy resolution for the sample at $g = 31\%$ ($R^2 = 0.992$).

Furthermore, compared with the seed side, the Ga concentration decreased toward the tail side of the crystal, which increased the ionization barrier at the $5d_1$ level and the intensity of the emission peak.

Figure 4a shows the pulse-height spectra measured at various positions using a ^{137}Cs excitation source (662 keV). The calculated light yields and energy resolutions based on this pulse-height spectra results are listed in Table 1. The light yield was determined by comparison with a mirror-polished 5 mm × 5 mm × 1 mm GAGG: Ce standard, which exhibits a light yield of 46,000 photons/MeV and an emission peak of 507 nm[11]. The YAGG: Ce, Mg samples exhibited a light yield of 46,700 photons/MeV, which is nearly identical to that of the standard GAGG crystal. Though the light yield slightly decreased with increasing solidification fraction, the uniformity of the light yield along with the growth direction was confirmed, demonstrating that the crystal is homogeneous in light yield throughout its entire length. Furthermore, the energy resolution was calculated using the following function based on the pulse-height spectra:

$$y = y_0 + y_1 x + y_2 x^2 + \frac{A}{\omega_1 \sqrt{\frac{\pi}{2}}} exp\left\{-2\left(\frac{(x - x_c)}{\omega_1}\right)^2\right\} + \frac{B}{\omega_2 \sqrt{\frac{\pi}{2}}} exp\left\{-2\left(\frac{(x - C * x_c)}{\omega_2}\right)^2\right\}$$

Because the pulse-height spectrum contains three components (Compton scattering, energy escape caused by the K-absorption edge, and photoelectric absorption), it was fitted using an approximated function expressed as

Sample	Light yield (Photons/MeV)	Energy resolution (%)	1st decay time (ns) /ratio (%)	2nd decay time (ns) /ratio (%)
Cz-GAGG(STD)	46,000	7.2	84 / 95	309 / 5
g = 1%	46,700	9.9	51 / 97	199 / 3
g = 9%	45,100	8.5	44 / 77	92 / 23
g = 15%	45,000	9.2	47 / 90	96 / 10
g = 23%	46,400	8.5	42 / 62	72 / 38
g = 31%	44,500	8.8	33 / 34	57 / 66
g = 37%	44,800	11.4	30 / 31	55 / 69
g = 45%	42,900	-	25 / 30	54 / 70

Table 1. Calculated light yields, energy resolutions, and scintillation decay times at various positions for YAGG: Ce, Mg single crystal scintillators.

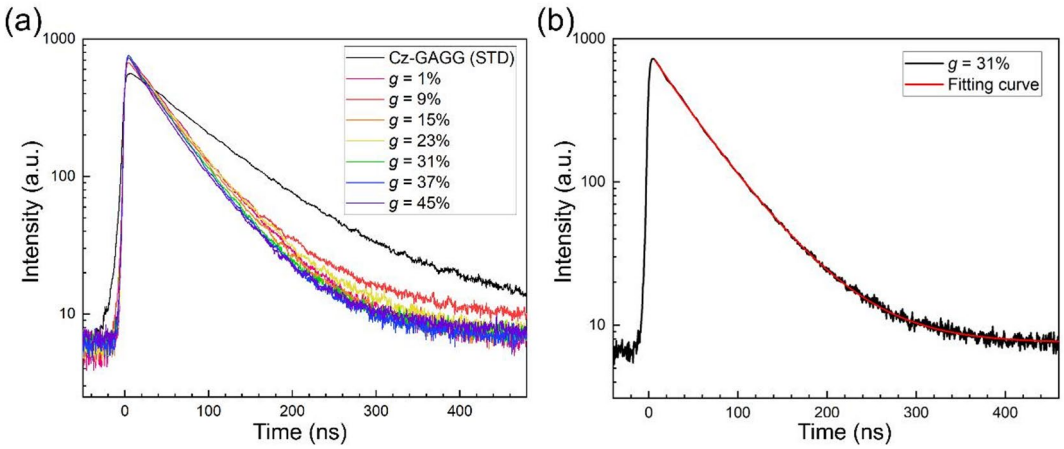

Fig. 5. (**a**) ^{137}Cs-induced scintillation decay curves of YAGG: Ce, Mg at various positions. (**b**) Fitting results of the scintillation decay curve for the sample at $g = 31\%$ ($R^2 = 0.999$).

the superposition of a second-order polynomial function and two Gaussian functions[38–40]. The function outputs y for each input x (MCA channel), where y_1, y_2, A, and B are constant, and x_c represents the x value of the peak position. The constant C is a correction factor that ensures that the peak x value corresponds to the position of the K-absorption edge of the host atom. Given that the K-absorption edge of the host atom Y is 17 keV, the value of C was set to (662 keV − 17 keV)/662 keV = 0.974. Then, energy resolution was calculated with the parameter of ω_1 obtained from Gaussian1 and the equation that $\Delta E/E = (FWHM/xc) \times 100\%$, $(FWHM = \sqrt{2ln2}\omega\ 1)$. Figure 4b shows the fitting results for the energy resolution at g = 31%. The energy resolution varied from 8.5% to 11.4% throughout the crystal. In addition, it degraded on the tail side (g = 37% and 45%), corresponding to a decrease in light yield.

Figure 5a shows the scintillation decay time measurements of the sample under ^{137}Cs excitation at various positions. The case of g = 31% is shown in Fig. 5b as a representative example of the spectral fitting. The scintillation decay times calculated from double exponential fitting are summarized in Table 1. At all positions, both the first and second decay components exhibit shorter scintillation decay times than those of GAGG: Ce[21]. In addition, the scintillation decay time on the tail side is shorter than that on the seed side. The ICP-AES results indicate that the Mg concentration was 0.176 at% on the seed side (g = 1%) and 0.220 at% on the tail side (g = 45%). The observed shortening of the decay time is considered correlated with the elevated Mg concentration[41].

Figure 6a shows the measured afterglow curves compared with the standard BGO scintillator. An extremely low afterglow level was achieved owing to the stabilization of Ce^{4+} by the Mg^{2+} co-dopant, which prevented the localization of electrons from the conduction band in traps, thereby decreasing the delayed luminescence phenomenon[22,31,42]. Figure 6b shows the comparison of afterglow levels among the YAGG: Ce, Mg seed (Fig. 6a) and commercial GAGG: Ce and YAG: Ce samples from CRYTUR company. It is clear that YAGG: Ce, Mg perform the best having an average value of afterglow within 10-20ms after X-ray cut-off around 280 and 640 ppm for g = 1% and 45%, respectively, while GAGG: Ce, Mg and YAG: Ce commercial standards from CRYTUR show values of 510 ppm and 1000 ppm, respectively. The increased presence of Ce^{4+} is further confirmed by the absorption spectra in Fig. 7 where the charge transfer absorption of Ce^{4+} is evident below 350 nm.

Scintillation mechanism in YAGG: Ce, Mg crystal is somewhat different with respect to classical YAG: Ce (LuAG: Ce) crystals and multicomponent GAGG: Ce ones as well. In the former crystals grown from the melt the stabilization of Y(Lu) at the octahedral Al site (called an antisite defect) occurs which creates a shallow electron trap detrimental in transfer stage of scintillation mechanism which was studied mainly in LuAG: Ce[43].

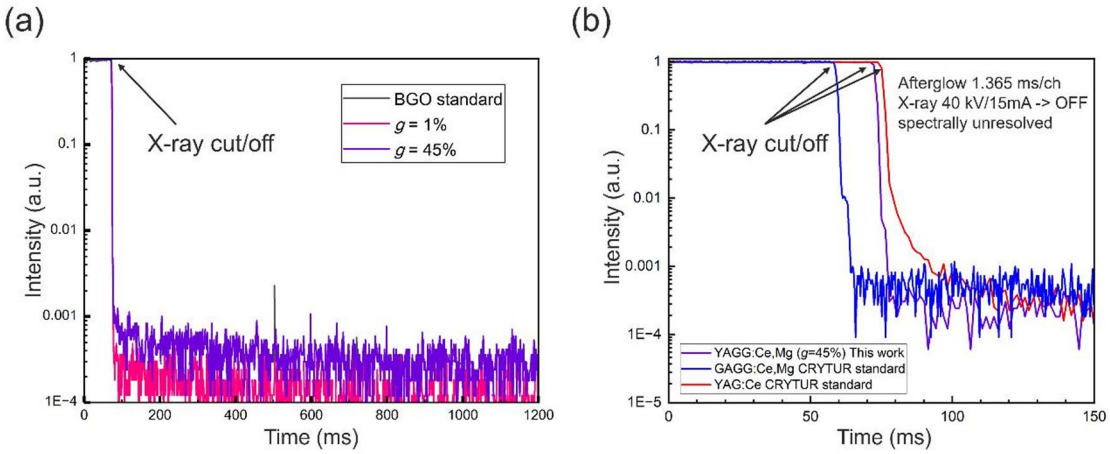

Fig. 6. (**a**) Afterglow curves of YAGG: Ce, Mg seed and tail samples compared with the BGO standard. (**b**) Afterglow curve of YAGG: Ce, Mg tail samples compared with GAGG: Ce, Mg and YAG: Ce, which are representative multicomponent garnet crystals.

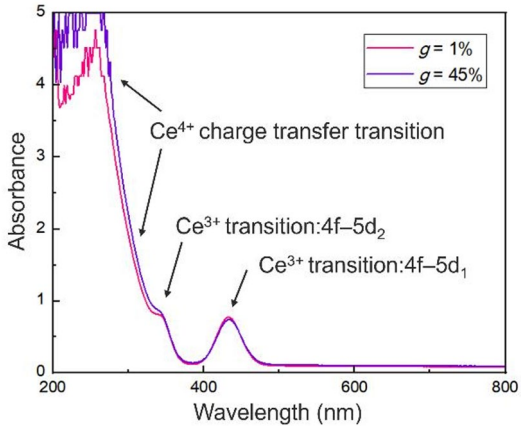

Fig. 7. Absorbance spectra of YAGG: Ce, Mg samples.

Furthermore, the trapped exciton around this antisite defect gives rise to a UV emission band which competes with Ce^{3+} emission center and negatively influences scintillation response as UV emission is far slower compared to Ce^{3+} one[44]. The admixture of Ga into LuAG: Ce was shown to prevent the trapping of free carriers due to the mentioned shallow traps as it lowers the bottom of conduction bands such that the energy level of shallow traps is no longer in the forbidden gap[45]. This leads also to destabilization of exciton trapping at antisite defect, i.e. to diminishing of unwanted UV emission in the Ga-admixed LuAG crystal[46]. The present study of YAGG: Ce crystal shows the same effect also in the Ga-admixed YAG host: UV emission is not present at all (Fig. 3) while it is routinely observed in YAG: Ce and LuAG: Ce radioluminescence spectra at RT[47]. In GAGG: Ce, part of the energy of the incoming ionization radiation absorbed in the host lattice is transferred to the Ce^{3+} centers through the Gd-sublattice[48] which causes slower components in the scintillation response. Such a negative feature is not present in YAGG: Ce crystal. Finally, due to favorable segregation coefficient of both the cerium and magnesium ions in YAGG lattice we achieved the acceleration of scintillation response below the photoluminescence decay time of Ce^{3+} (about 50-55ns in YAGG host) which is explained by the quenching effect in closely spaced Ce-Mg pairs analogously to heavily doped GAGG: Ce, Mg[49]. Summarising, given the above description the YAGG host appears the most favorable in comparison with YAG, LuAG and GAGG ones in terms of fast and efficient energy transfer towards cerium emission centers in scintillation mechanism which is further reflected also in its ultralow afterglow demonstrated in Fig. 6.

Conclusions

In this study, the Cz growth of YAGG: Ce, Mg single crystals were investigated. As initially anticipated, pronounced evaporation of gallium oxide occurred, leading to oxidation of the iridium crucible and subsequent deposition of iridium metallic films on the melt surface. These effects significantly hindered stable crystal growth in the early stages of this study. Based on these findings, optimization of the growth atmosphere and other

growth conditions were undertaken. The mitigation of gallium oxide evaporation, which effectively eliminated iridium deposition on the melt surface, enabled the successful Cz growth of the YAGG: Ce, Mg single crystal up to solidification fraction of 45%.

The grown YAGG: Ce, Mg achieved a light yield of 46,700 photons/MeV, energy resolution of 8.5 ~ 11.4% at 662 keV, low afterglow, and a fast decay time of approximately 50 ns, which are comparable to or surpass those of GAGG: Ce, Mg. Furthermore, the variation in light yield up to a solidification fraction of 45% was limited to 8.5%, and the afterglow remained below the 640 ppm level. Our analysis indicates that the uniformity of scintillation properties within the grown crystal correlates with the compositional homogeneity of the constituent elements and dopants. In conclusion, compared with the currently used GAGG: Ce, Mg scintillator for PCCT, we have demonstrated that a scintillator with higher light yield, superior afterglow characteristics, and no adverse effects from the Gd escape peak can be grown as a YAGG: Ce, Mg bulk crystal by the Cz method while maintaining uniformity in its scintillation properties. In particular, the market price of iridium metal has surged by an order of magnitude in recent years, creating a major cost challenge for the mass production of oxide scintillators. Degradation of Ir crucibles has been a critical factor limiting the practical application and large-scale manufacturing of these crystals. In this study, we demonstrated that Cz growth using Ir crucibles can be conducted while suppressing crucible deterioration associated with gallium oxide evaporation. These achievements represent a significant step toward the practical realization and industrial deployment of YAGG: Ce, Mg scintillators.

Further improvement in scintillator performance, particularly in energy resolution, can be expected for YAGG: Ce, Mg through optimization of the Ce and Mg doping concentrations, as well as advancements in crystal scaling and quality. Moreover, for YAGG: Ce, Mg, increasing the oxygen partial pressure of the atmosphere during growth to further suppress gallium oxide evaporation is expected to improve mass producibility, enabling larger-diameter crystals and higher solidification yields while maintaining uniform scintillation properties. Notably, our research group has been developing a novel melt growth method, called Oxide Crystal Growth from a Cold Crucible (OCCC), to grow over 2 inch diameter bulk single crystals without using precious metal crucibles[50]. In the OCCC method, Ir crucibles are not required, making it possible to grow oxide crystals even under a 100% oxygen atmosphere. Future studies will focus on growing YAGG: Ce, Mg single crystals using the OCCC method.

Data availability

The datasets used and/or analysed during the current study are available from the corresponding author on reasonable request.

Received: 22 September 2025; Accepted: 4 December 2025
Published online: 20 January 2026

References

1. Gutjahr, R. et al. Human imaging with photon counting–based computed tomography at clinical dose levels: contrast-to-noise ratio and cadaver studies. *Invest. Radiol.* **51**, 7, 421–429 (2016).
2. Flohr, T. et al. Photon-counting CT review. *Phys. Med.* **79**, 126–136 (2020).
3. Alessio, A. M. & Lawrence, R. M. Quantitative material characterization from multi-energy photon counting CT. *Med. Phys.* **40.3**, 031108 (2013).
4. Rau, A. et al. Photon-counting computed tomography (PC-CT) of the spine: impact on diagnostic confidence and radiation dose. *Eur. Radiol.* **33**, 5578–5586 (2023).
5. Symons, R. et al. Low-dose lung cancer screening with photon-counting CT: a feasibility study. *Phys. Med. Biol.* **62**, 202–213 (2017).
6. Shimazoe, K. et al. An energy-resolving photon-counting X-ray detector for computed tomography combining silicon-photomultiplier arrays and scintillation crystals. *Commun. Eng.* **3**, 167 (2024).
7. Shimazoe, K., Kim, C., Takahashi, H. & Arai, Y. Design improvement and characterization of SOI-based silicon-photomultiplier prototype. *Nucl. Instrum. Methods Phys. Res. A*. **1047**, 167902 (2023).
8. Shimazoe, K. et al. Development of simultaneous PET and Compton imaging using GAGG-SiPM based pixel detectors. *Nucl. Inst. Methods Phy Res. Sec A: Acc. Spec. Det as Equ*. **954**, 161499 (2020).
9. Taguchi, K. et al. Imaging performance of a LaBr3: Ce scintillation detector for photon counting x-ray computed tomography: simulation study. *Med. Phys.* **52** (1), 158–170 (2025).
10. Van der Sar, S. J., Brunner, S. E. & Schaart, D. R. Silicon photomultiplier-based scintillation detectors for photon-counting CT: A feasibility study. *Med. Phys.* **48**, 6324–6338 (2021).
11. Kamada, K. et al. Development of a prototype detector using APD-arrays coupled with pixelized ce: GAGG scintillator for high resolution radiation imaging. *IEEE Trans. Nucl. Sci.* **61**, 348–352 (2014).
12. Kamada, K. et al. Composition engineering in Cerium-Doped $(Lu,Gd)_3(Ga,Al)_5O_{12}$ Single-Crystal scintillators. *Cryst. Growth Des.* **11**, 4484–4490 (2011).
13. Kochurikhin, V. et al. Czochralski growth of 4-inch diameter ce: $Gd_3Al_2Ga_3O_{12}$ single crystals for scintillator applications. *J. Cryst. Growth.* **531**, 125384 (2020).
14. Kamada, K. et al. Large size Czochralski growth and scintillation properties of Mg^{2+} Co-doped Ce:$Gd_3Ga_3Al_2O_{12}$. *IEEE Trans. Nucl. Sci.* **63**, 443–447 (2016).
15. Tuccori, N. & Peeters, S. J. Photon-counting computed tomography and scintillator-based detectors: a simulation analysis with scintillating and reflecting materials currently on the market. *IEEE Trans. Nucl. Sci.* **70**, 1404–1412 (2023).
16. Bushberg, J. T., Seibert, J. A., Leidholdt, E. M. & Boone, J. M. *The Essential Physics of Medical Imaging* 3rd edn (Lippincott Williams & Wilkins, 2011).
17. Singh, S. & Singh, D. Down-conversion and structural characterizations of trivalent terbium-doped Garnet nanocrystalline phosphors for lighting applications. *J. Mater. Sci. Mater. Electron.* **32**, 17674–17685 (2021).
18. Omuro, K. et al. Tailoring scintillation and luminescence through Co-doping engineering: A comparative study of Ce, Tb Co-doped YAGG and GAGG Garnet crystals. *J. Alloys Compd.* **1008**, 176550 (2024).
19. Omuro, K. et al. Insights into luminescence and energy transfer processes in Ce^{3+} and Tb^{3+} co-doped $(Gd, Y)_3Al_2Ga_3O_{12}$ Garnet single crystals. *J. Lumin.* **273**, 120663 (2024).

20. Omuro, K. et al. Crystal growth and characterization of 1-inch GTAGG: Ce single crystal for sub-micron resolution synchrotron radiation X-ray imaging. *Sci. Rep.* **15**, 12993 (2025).
21. Berger, M. J. et al. XCOM: Photon cross section database (version 1.5) (2010).
22. Kamada, K. et al. Mg co-doping effects on Ce doped Y3(Ga,Al)5O12 scintillator. *IOP Conf. Ser. Mater. Sci. Eng.* **169**, 012030 (2017).
23. Zheng, R. et al. Study on the inhomogeneity of LYSO crystal boules grown by the CZ method for PET applications. *J. Cryst. Growth.* **546**, 125708 (2020).
24. Yoshikawa, A. et al. Czochralski growth of 2 in. Ce-doped (La, Gd) 2Si2O7 for scintillator application. *J. Cryst. Growth.* **452**, 57–64 (2016).
25. Kuwano, Y. et al. Crystal growth and properties of (Lu, Y) 3Al5O12. *J. Cryst. Growth.* **260**, 159–165 (2004).
26. Abell, J. S. et al. An investigation of phase stability in the Y2O3-Al2O3 system. *J. Mater. Sci.* **9** (4), 527–537 (1974).
27. Nicolas, J. et al. Sm2O3 Ga2O3 and Gd2O3 Ga2O3 phase diagrams. *J. Solid State Chem.* **52** (2), 101–113 (1984).
28. Kamada, K. et al. Growth of 2-inch size ce: doped Lu2Gd1Al2Ga3O12 single crystal by the Czochralski method and their scintillation properties. *J. Cryst. Growth.* **410**, 14–17 (2015).
29. Yoshikawa, A. & Valery, C. Growth of optical crystals by the micro-pulling-down method. *MRS Bull.* **34** (4), 266–270 (2009).
30. Kamada, K. et al. Alkali Earth co-doping effects on luminescence and scintillation properties of Ce doped Gd3Al2Ga3O12 scintillator. *Opt. Mater.* **41**, 63–66 (2015).
31. Kamada, K. et al. Single crystal growth of Ce:$Gd_3(Ga,Al)_5O_{12}$ with various Mg concentration and their scintillation properties. *J. Cryst. Growth.* **468**, 407–410 (2017).
32. Galazka, Z. Growth of bulk β-Ga2O3 single crystals by the Czochralski method. *J. Appl. Phys.* **131**, 031103 (2022).
33. Dean, J. A. *Lange's Handbook of Chemistry* (McGraw-Hill, 1999).
34. Yamaguchi, H. et al. Effects of Mg-codoping on luminescence and scintillation properties of Ce doped $Lu_3(Ga,Al)_5O_{12}$ single crystals. *Opt. Mater.* **65**, 60–65 (2017).
35. Ogiegło, J. M. et al. Luminescence and luminescence quenching in $Gd_3(Ga,Al)_5O_{12}$ scintillators doped with Ce^{3+}. *J. Phys. Chem. A.* **117**, 2479–2484 (2013).
36. Chen, X. et al. Effects of Ga substitution for al on the fabrication and optical properties of transparent Ce:GAGG-based ceramics. *J. Eur. Ceram. Soc.* **37**, 4109–4114 (2017).
37. Kamada, K. et al. Scintillator-oriented combinatorial search in the Ce doped (Y,Gd)3(Ga,Al)5O12 multicomponent Garnet compounds. *J. Phys. D: Appl. Phys.* **44**, 505104 (2011).
38. Iredale, P. The effect of the non-proportional response of NaI (Tl) crystals to electrons upon the resolution for γ-rays. *Nucl. Instrum. Methods.* **11**, 340–346 (1961).
39. Prescott, J. R. & Narayan, G. H. Electron responses and intrinsic line-widths in NaI (Tl). *Nucl. Instrum. Methods.* **75**, 51–55 (1969).
40. Sibczynski, P. et al. Characterization of GAGG: Ce scintillators with various Al-to-Ga ratio. *Nucl. Instrum. Methods.* **772**, 112–117 (2015).
41. Bartosiewicz, K. et al. A study of Mg^{2+} ions effect on atoms segregation, defects formation, luminescence and scintillation properties in Ce^{3+} doped $Gd_3Al_2Ga_3O_{12}$ single crystals. *J. Alloys Compound.* **905**, 164154 (2022).
42. Nikl, M. et al. Defect engineering in Ce-doped aluminum Garnet single crystal scintillators. *Cryst. Growth Des.* **14**, 4827–4833 (2014).
43. Nikl, M. et al. The antisite Lu_{Al} defect-related trap in $Lu_3Al_5O_{12}$:Ce single crystal. *Phys. Stat. Sol (b).* **242**, R119–R121 (2005).
44. Nikl, M. et al. Energy transfer to the Ce^{3+} centers in $Lu_3Al_5O_{12}$:Ce scintillator. *Phys. Stat. Sol.* **201**, R41-R44 (2004).
45. Fasoli, M. et al. Band gap engineering for shallow trap removal in $RE_3Al_5O_{12}$ garnets. *Phys. Rev. B* **84**, 081102(R) (2011).
46. Ogino, H. et al. Growth and optical properties of $Lu_3(Ga,Al)_5O_{12}$ single crystals for scintillator application. *J. Cryst. Growth.* **311**, 908–911 (2009).
47. Nikl, M. et al. Development of LuAG-based scintillator Crystals - A review. *Progr Cryst. Growth Charact. Mater.* **59**, 47–72 (2013).
48. Khanin, V. et al. Exciton interaction with Ce3 + and Ce4 + ions in $(LuGd)_3(Ga, Al)_5O_{12}$ ceramics. *J. Lumin.* **237**, 118150 (2021).
49. Martinazzoli, L. et al. Compositional engineering of multicomponent Garnet scintillators: towards an ultra-accelerated scintillation response. *Mater. Adv.* **3**, 6842–6852 (2022).
50. Yoshikawa, A. et al. Bulk Single-Crystal growth of Ce/$Gd_3(Al,Ga)_5O_{12}$ from melt without a precious metal crucible by pulling from a cold container. *Cryst. Growth Des.* **23**, 2048–2054 (2023).

Acknowledgements

We would like to thank the following people for their support: Mr. Issei Narita of the Cooperative Research and Development Center for Advanced Materials, Tohoku university, Mr. Fuyuki Sakamoto of the Analytical Research Core for Advanced Materials, Institute for Materials Research, Tohoku University, Mr. Yoshihiro Nakamura of the Institute of Multidisciplinary Research for Advanced Materials (IMRAM), Tohoku University.

Author contributions

H.S. conducted all aspects of this study, including conceptualization, methodology, resources, investigation, formal analysis, data curation, and visualization, and drafted the original manuscript. K.K contributed to funding acquisition and investigation, with a primary focus on crystal growth. L.G. contributed to crystal growth and the provision of materials. M.Y., K.J.K., S.I and R.M. provided methodology and resources. A.B. contributed to evaluation and interpretation of the optical measurement data. M.N. contributed to funding acquisition and investigation, with a primary focus on luminescence mechanism. A.Y. supervised the project. All authors reviewed and edited the manuscript.

Funding

This work was partially supported by JSPS KAKENHI, Grant No. 19H00672, 20K20488, 22H04961, 19H00881, 19K1262 and JST CREST, Grant No. JPMJCR2331. This work was also partially supported by the JAEA Nuclear Energy S&T and Human Resource Development Project Grant Number JPJA23P23813521. Partial support from Operational Programme Johannes Amos Comenius financed by European Structural and Investment Funds and the Czech Ministry of Education, Youth and Sports (Project No. SENDISO -CZ.02.01.01/00/22_008/0004596) is acknowledged with thanks. This work was also partially supported by Go-Tech Program (Support Industry Program) of the Ministry of Economy, Trade and Industry (METI), Japan.

Declarations

Competing interests
The authors declare no competing interests.

Additional information
Correspondence and requests for materials should be addressed to H.S. or K.K.

Reprints and permissions information is available at www.nature.com/reprints.

Publisher's note Springer Nature remains neutral with regard to jurisdictional claims in published maps and institutional affiliations.